Film Thickness Dependence of Surface and Internal Morphology Evolution in Polymer-Grafted Nanocomposites

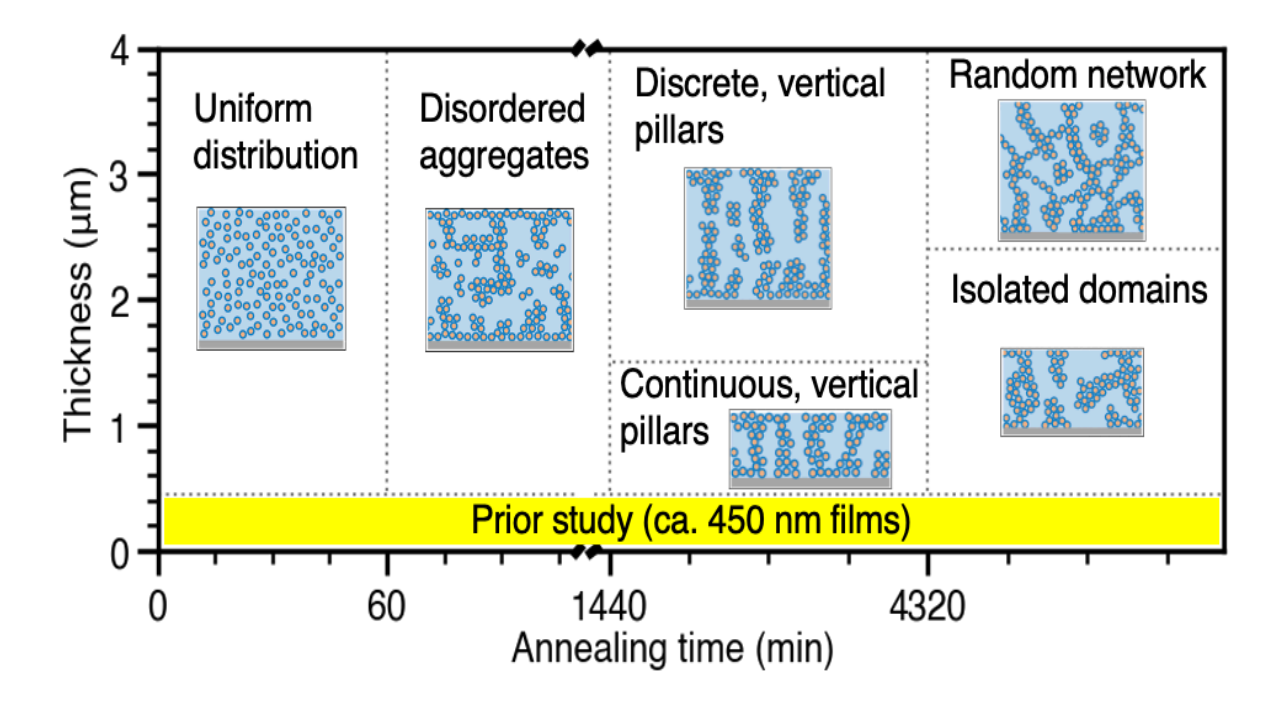
Aria C. Zhang¹, Kohji Ohno², Russell J. Composto¹*

¹ Department of Materials Science and Engineering, University of Pennsylvania, Philadelphia, 19104, USA

²Department of Materials Science, Graduate School of Engineering, Osaka Metropolitan University, Sakai, Osaka, 599-8531, Japan

* Corresponding author: composto@seas.upenn.edu

For Table of Contents Use Only



ABSTRACT

This study investigates the interplay between film thickness and the surface and internal morphologies in polymer nanocomposite (PNC) films. The PNC is 25 wt.% poly(methyl methacrylate)-grafted silica nanoparticles (NPs) in poly(styrene-ran-acrylonitrile) annealed in the two-phase region. At greatest confinement (120 nm), NP surface density remains constant and lateral phase separation is inhibited upon annealing. For thicker films (240 nm to 1400 nm), surface density increases with time before approaching ca. 740 NP/ μ m², consistent with 2D random close packing. Moreover, lateral domain growth exhibits a dimensional crossover as thickness increases from $t^{1/2}$ to $t^{1/3}$, consistent with domain coalescence. Water contact angles decrease upon annealing in agreement with the lateral domain composition. For thickest films (1400 nm to 4000 nm), a morphology map summarizes the distinct internal arrangements of NPs: disordered aggregates, continuous vertical pillars, discrete vertical pillars, isolated domains, and random networks. This study of PNC films provides guidance for controlling surface and bulk structure which can lead to improved barrier, mechanical and transport properties.

INTRODUCTION

Polymer nanocomposites (PNCs) typically consist of a polymer matrix mixed with nano-sized fillers. The addition of inorganic nanoparticles (NPs) enables PNCs to exhibit synergistic properties that are not accessible to traditional polymers, leading to materials of interest for a broad range of functions, such as enhanced mechanical performance, gas barrier and separation, catalysis, drug delivery, and capacitors and insulators. 1-8 The correlation between PNC properties and the spatial arrangement of NPs has been well established. In the past few decades, research has been performed to investigate how various parameters affect PNC structures, and in turn their macroscale properties. 10-12 However, because of the vast combinations of material parameters and processing conditions, the structure-property relationship in PNC films requires further investigation, particularly when film confinement plays a role. For example, the structure of a PNC depends on NP characteristics including size, shape, surface chemistry, molecular weight, and grafting density as well as matrix characteristics including type (e.g., homopolymer versus block polymer), structure (e.g., linear versus bottlebrush), and molecular weight. Surface and bulk structure also depends on the ratio of components as well as processing conditions (e.g., temperature and time), external fields (e.g., mechanical, electric, magnetic), and film thickness. Further understanding of these materials characteristics and processing conditions, both alone and in combination, is crucial in determining the final properties of PNC coatings.

Polymer brushes have been grafted to the surface of NPs to modulate the NP-matrix interaction. Polymer brushes not only can improve the dispersion of NPs in a matrix but also can introduce complex phase behavior that depends on the brush-matrix interactions. These interactions can be tailored by selecting from a diverse range of brush and matrix combinations. ^{13,14} Polymer brushes that are chemically similar to the matrix have been widely

studied. In this athermal case, parameters like NP size, confinement, grafting density, and relative chain length of the brush and matrix, lead to various structures, which in turn yield different optical and thermal properties. Notably, for densely grafted NPs in their athermal matrix, the transition from wet to dry brush occurs when the ratio of matrix to brush chain length is between 4 and 5.17-19 For sparsely grafted NPs, various structures like spherical aggregates, strings, and sheets form as a result of balancing the core-core attractions and brush dynamics. Under the matrix is chemically distinct from the brush, simulations and experiments show that the enthalpic interactions between the brush and matrix chains lead to phase separation in a similar fashion as the binary blends of their linear polymer counterparts. Koski et al. predicted phase diagrams of a PNC system using theoretically informed Langevin dynamics (TILD) and experimentally confirmed the prediction using silica NPs grafted with poly(methyl methacrylate) (PMMA) in a polystyrene (PS) matrix. Using TILD, Santos and Frischknecht predicted the phase behavior of binary and ternary PNC systems, consistent with experiments and modeling.

In addition to bulk morphology, the surface of polymer blend films can exhibit unique properties that provide insight into PNC behavior.^{25,26} For example, Jones et al. first observed surface-directed spinodal decomposition (SDSD) in isotopic binary polymer blends as a result of preferential attraction of the surface for one of the components.²⁶ Since then, decades of research have been devoted to investigating the surface and confinement effects on polymer blend films as these factors play an important role in the evolution of morphologies.^{27–31} Similarly, confinement is expected to influence the phase behavior and morphology of PNCs. Zhang et al. observed that confinement induced by topography patterns can lead to long-range, submicron domains with densely distributed PS-grafted gold NPs in a PMMA matrix.²¹ Chandra et al.

demonstrated that film thickness-induced confinement enhances the dispersion of polymer-grafted gold NPs in an athermal homopolymer matrix which leads to a significant decrease in glass transition temperature.³² However, a comprehensive study of the relationship between confinement and surface and bulk morphologies is lacking in PNC films.

Maguire et al. demonstrated that a PNC consisting of PMMA-grafted silica NPs (PMMA-NPs) in poly(styrene-ran-acrylonitrile) (SAN) exhibits a lower critical solution temperature (LCST) analogous to a PMMA/SAN blend.³³ Upon annealing in the two-phase region of the phase diagram, PMMA-NP/SAN films form a tri-layer structure, with a SAN-rich phase sandwiched between PMMA-NP wetting layers on the surface and substrate. In the SAN-rich phase, PMMA-NP pillars form, oriented perpendicular to the sample surface and spanned the film's thickness. Compared to the well-dispersed PMMA-NP case, the hardness and reduced modulus increased for the percolated PMMA-NP structures.³³ However, these studies were limited to films with a thickness of ca. 450 nm. A study by Chung et al. showed that PMMA/SAN films exhibit distinct morphologies, attributed to confinement, as a function of film thickness.³⁴ To effectively design PNC films with attractive properties, understanding the relationship between film thickness and morphology is important. Specifically, we address how confinement, introduced by decreasing film thickness, affects the surface morphology of PMMA-NPs, and whether there is a thickness threshold above which the arrangement of PMMA-NPs can no longer stabilize PNC films.

Here, we systematically investigate the surface and bulk morphologies of PNC films to determine how morphology depends on film thicknesses from 120 nm to 4000 nm. These PNC films, 120 nm to 4000 nm in thickness, contain 25 wt.% PMMA-NPs mixed in a SAN matrix and are annealed in the two-phase region of the phase diagram at 190°C. To study surface structure,

films are characterized using atomic force microscopy (AFM), water contact angle measurement, and time-of-flight secondary ion mass spectrometry (ToF-SIMS). Upon annealing, films thicker than 240 nm are observed to form distinct PMMA-NP-rich and SAN-rich domains at the surface. This lateral phase separation is accompanied by an increase in the areal density of NPs at the surface which approaches a value consistent with 2-dimensional (2D) random close packing (RCP) of hard spheres. By contrast, thinner 120 nm films only display height fluctuations. These films also exhibit a reduction in the surface density of NPs, which is partly attributed to minimizing the density gradient of NPs near the surface. 32,35 For 520 nm and 1400 nm films, the lateral domain growth quantified by the correlation length, ς , initially scales with $t^{1/3}$, consistent with diffusive droplet coalescence. At longer times, ς stabilizes at ca. 650 nm due to the kinetic trapping of PMMA-NPs. A dimensional crossover from $t^{1/3}$ to $t^{1/2}$ is observed for thicknesses near 240 nm and attributed to suppression of surface-directed spinodal decomposition. Water contact angles on PNC films decrease with annealing time and agree with the area fractions of PMMA-NP-rich and SAN-rich domains. NP surface excesses from ToF-SIMS are congruent with NP areal density from AFM. Further, NP diffusion coefficients are in good agreement with previous measurements.³⁶

To complement surface studies, the bulk morphology of PNC films is investigated. Previously, ca. 450 nm films at the same composition displayed vertical PMMA-NP pillars that span the PMMA-NP surface and substrate wetting layers. One goal of the present study is to determine the thickness threshold above which vertical pillars no longer form. To address this challenge, cross-sections of films with thicknesses of 1400 nm, 2400 nm, and 4000 nm were characterized using transmission electron microscopy (TEM). A morphology map was constructed to summarize the relationship between the bulk structure and film thickness as a

function of annealing time. Six distinct regimes were identified based on NP arrangement: uniform distribution, disordered aggregates, continuous vertical pillars, discrete vertical pillars, encapsulated domains, and random networks. Taken together, these studies of the surface and bulk morphologies provide a roadmap for manipulating the PNC structure-property relationship across a large parameter space. These new observations can lead to improved performance for applications requiring durable barrier coatings.³⁷ Further, the percolated structures provide a foundation for designing materials with attractive electric and ion conductivity,^{38–40} crucial for the innovation of electronic and storage technologies as well as batteries.

RESULTS AND DISCUSSION

Lateral Phase Separation. To investigate surface topography, films of PMMA-NPs mixed with SAN at a 25/75 weight ratio were characterized at thicknesses of 120 nm, 240 nm, 520 nm, and 1400 nm. Samples were prepared as described in the Materials and Methods section. AFM was performed to probe the initial state of as-cast PNC films. To assess bulk dispersion, TEM was performed on as-cast films of 120 nm and 240 nm (top-down view), and 1400 nm (cross-sectional view). Figure 1 presents the AFM height image and TEM image of the 120 nm as-cast film, along with a TEM image of the 1400 nm as-cast film. These images indicate a uniform distribution of PMMA-NPs across the surface (Figure 1a) and within the bulk (Figure 1b-c). The AFM image is representative of all thicknesses. The top-down TEM images are specific to 120 nm and 240 nm films, whereas the cross-sectional TEM image represents films thicker than 520 nm. The processing and analysis of the AFM height and top-down TEM images are described in the Supporting Information (Figure S1). For the as-cast 120 nm films, the average areal number density of the PMMA-NPs on the surface is 246 ± 7 particles/μm². Analysis of the AFM data yields a root mean square roughness (R_a) of 2.1 ± 0.1 nm. Notably,

the areal densities and R_q values are relatively consistent for as-cast films of various thicknesses in this study. The top-down TEM image revealed the average diameter of the SiO_2 core to be 13 \pm 5 nm, with a PDI of 1.6 calculated based on **Equation S2** in the Supporting Information.⁴¹ A histogram of the particle diameter and the corresponding Gaussian fit are shown in **Figure S2**. The observed particle diameter (13 \pm 5 nm) is smaller than the expected value (15 nm) ⁴² with a large standard deviation potentially due to the nature of the 3-dimensional projection on a 2-dimensional plane in the TEM images.

Figure 1. (a) AFM height image and (b) top-down TEM image of 120 nm as-cast PNC film with 25 wt.% PMMA-NPs. The root mean square roughness, R_q, of the height image is 2.1 0.1 nm. (c) A cross-sectional TEM image of the 1400 nm as-cast film.

Upon annealing at 190 °C, the surface morphology of the 120 nm and 240 nm films evolves. **Figure 2** shows the AFM and OM images of these films post-annealing at intervals of 1 h, 10 h, 24 h, and 72 h (or 168 h). For the thinnest film (120 nm), PMMA-NPs form a close-packed structure at the surface after 1 h, with a corresponding R_q decreasing from 2.1 ± 0.1 nm (as-cast) to 0.8 ± 0.1 nm. Extended annealing (10 h and 24 h) leads to height fluctuations with higher PMMA-NP-rich regions (bright) and lower SAN-rich regions (dark). Note that these fluctuations (ca. 5 nm) are much less than the hydrodynamic diameter of PMMA-NP (38 nm). After 72 h, the

120 nm film dewets due to the thermal nucleation of holes, 43 indicating that the PMMA-NPs are unable to prevent hole growth as shown in Figure 2d. In Figure 2d, the blue circular areas represent dewetted holes with a diameter of ca. 60 ± 8 µm. The silicon substrate within these holes is covered by approximately 24 nm of a residual PNC film, as determined by AFM line scans at the edge of the holes (not shown). Within the holes, height profiles reveal an array of PMMA-NPs that constitutes approximately 85% of the total area, with an average center-to-center interparticle distance of 39 ± 7 nm as shown in Figure S3. Similar to the 120 nm films, the 240 nm films exhibit local height fluctuations after 1 h, as shown in **Figure 2e**. However, unlike the 120nm case, the morphology continues to evolve into a phase-separated structure with continuous PMMA-NP-rich domains (bright) surrounding discrete SAN-rich domains (dark) after 10 h, as shown in Figure 2f. After 72 h, both domains coarsen and grow patchy (not shown). As shown in Figure 2h, films annealed for up to 168 h are stable. Compared to stable 240 nm films, the 120 nm films only remain stable up to 24 h. Film integrity is breached between 24 h and 72 h as kinetic trapping is ultimately overcome by fluctuations, consistent with dewetting studies of PMMA/SAN films.44

Figure 2. AFM height and OM images of 120 nm (a-d) and 240 nm (e-h) PNC films annealed at 190 °C for 1 h, 10 h, 24 h, and 72 h (or 168 h). The dimension of the AFM images is 2 μm 2 μm. Bright dots (higher) represent the NP core, whereas darker regions (lower) are SAN-rich. For the 120 nm film at 72 h, the OM image (d) shows film dewetting (blue holes). The scale bars for all AFM images are 400 nm. The height scale is chosen to optimize the distinction between particles. Images with dashed and solid boxes represent conditions where height fluctuations and phase separation dominate, respectively.

As shown in **Figure 3**, thicker films (520 nm and 1400 nm) exhibit similar but faster lateral phase separation than the 240 nm films. After 1 h, the 520 nm film morphology is dominated by height fluctuations that result in higher PMMA-NP-rich regions separated by lower PMMA-NP-poor regions, as shown in **Figure 3a**. Subsequently, these films undergo phase separation with a distinct boundary between nearly pure PMMA-NP domains and SAN domains after 3 h. Qualitatively, both domains continue to coarsen with longer annealing times as shown

in **Figure 3c-d**. The thicker 1400 nm films undergo film separation more rapidly, after only 1 h, and exhibit qualitatively similar morphologies as the 520 nm film after 3 h. In conclusion, thicker films (520 nm and 1400 nm) exhibit a faster onset of phase separation than thinner films (240 nm).

Figure 3. AFM height images of 520 nm (top row) and 1400 nm (bottom row) PNC films annealed at 190 °C for 1 h, 3 h, 72 h, and 168 h. The dimension of the AFM images is 2 μm 2 μm. The scale bars are 400 nm. The height scale is adjusted to optimize the distinction between NP rich and NP poor regions. Images with dashed and solid boxes represent conditions where height fluctuations and phase separation dominate, respectively.

To quantify surface segregation, the average areal density of PMMA-NPs was measured from AFM images for 120 nm and 240 nm films and plotted as the square root of annealing time as shown in **Figure 4**. For both cases, the areal density increases rapidly and approaches a constant value. Although data in the initial growth regime is limited, this behavior is consistent

with a diffusion-limited process where the diffusion coefficient can be estimated (detailed in a later section using ToF-SIMS). The timestamps labeled at the top of **Figure 4a**, as well as in selected subsequent figures, correspond to the annealing time for the data point below them. For 120 nm films, PMMA-NPs reach a nearly constant areal density of approximately 605 ± 6 particles/μm² after 1 h. This value falls short of the theoretical maximum of 740 particles/μm² (dotted line), calculated from a "hard sphere" 2D random close packing (RCP) model⁴⁵ (**Figure 4**, inset) using a hydrodynamic diameter of 38 nm.⁴⁴ In contrast, for 240 nm films, the areal density approaches this maximum density after 10 h and remains constant thereafter. For the 120 nm film, the lower areal density may be attributed to minimizing the NP concentration gradient and maximizing matrix chains at the surface.³² Following the Schmidt and Binder model, the bulk free energy of an AB polymer mixture in a semi-infinite system (z > 0) can be expressed as:

$$\frac{F_b}{k_B T} = \int dA \int_0^\infty dz \left\{ \frac{\varphi}{N_A} ln\varphi + \frac{1-\varphi}{N_B} ln(1-\varphi) + \chi \varphi (1-\varphi) - \Delta \mu \varphi + \left(\frac{a^2}{36\varphi (1-\varphi)} (\nabla \varphi)^2 \right) \right\}.$$
(1)

In **Equation 1**, α is the spacing of a cubic lattice, N_A (or N_B) is the degree of polymerization of polymer A (or B), φ is the volume fraction of polymer A, χ is the interaction parameter between polymers A and B, and $\Delta\mu$ is the chemical potential difference.^{35,46} The last term in **Equation 1**, known as the squared gradient term, accounts for the energy penalty due to concentration gradients across the film. Minimizing the gradient term ($\nabla\varphi$) perpendicular to the surface is important for reducing the total free energy of the system. Importantly, this gradient becomes steeper as NP confinement increases. In addition, for sufficiently thick PNC films, matrix chains are mainly isotropic near the surface. However, as the film thickness decreases, matrix chains tend to orient along the surface, reducing the available area for NPs and consequently decreasing

NP surface density.³² Given that 120 nm films correspond to only 3 to 4 layers of PMMA-NPs throughout the thickness, the effect of density gradient minimization and matrix chain packing is expected to be more pronounced compared to thicker films, leading to a reduced NP surface density.

For 240 nm films annealed for 10 h or longer, phase separation leads to the formation of densely packed PMMA-NP-rich domains (Figure 4b, top) with an areal density plotted in Figure 4a (open orange circles). Specifically, after 10 h, the areal density within these domains is ca. 930 particles/µm². Using a 2D RCP model (cartoon in Figure 4a), the corresponding effective diameter of PMMA-NPs in the densely packed domains is 34 nm. This value is consistent with the center-to-center interparticle distances measured from line scans such as that shown in Figure 4b, bottom. Compared to the hydrodynamic diameter of 38 nm, the smaller effective diameter suggests interdigitation of the PMMA brush. After 72 h, the areal density increases to 1050 particles/µm², corresponding to an effective diameter of approximately 32 nm, consistent with the center-to-center interparticle distance measured from AFM images (not shown). For comparison, the hard-core diameter of NPs is 13 ± 5 nm. These studies show that the areal density of the 120 nm films is slightly less than that found in the 240 nm films. Further, for the lateral phase separation observed in 240 nm films, the NP densities in the PMMA-NP-rich domains are about 40% greater than in the entire AFM images, including both NP-rich and SAN-rich domains.

Figure 4. (a) PMMA-NP areal number density as a function of square root of annealing time for 120 nm (blue square) and 240 nm films (orange circle). Open orange circles denote the areal density for 240 nm films. The dotted line at 740 particles/μm² is the theoretical maximum areal density, derived using a 2D random close packing model for hard spheres (inset) with a diameter of 38 nm. (b) An AFM height image of the 240 nm film at 10 h, with a corresponding height profile of the line scan indicated by the white line within a NP-rich domain in the height image. The height profile shows an average center-to-center (peak-to-peak) interparticle distance of 34 nm. Annealing times in (a, top) are included for text reference.

For 520 nm and 1400 nm films, the areal densities exhibit similar trends as that observed for the 240 nm films shown in **Figure 4**. **Figure 5** presents the average PMMA-NP areal densities across entire AFM height images (solid symbols) as well as the areal density in the PMMA-NP-rich domains (open symbols). **Figure 5** also shows areal densities from the 2D RCP model using hydrodynamic (38 nm, dotted line) and effective (32 nm, dashed line) diameters. For both thicknesses, the areal densities increase rapidly after 1 h, and at longer times approach 740 particles/µm² (dotted line). For the PMMA-NP-rich domains, areal densities gradually

approach the RCP prediction of 1044 particles/μm² (dashed line) after 72 h. These observations align with the morphological trends observed in **Figure 3** where brush interdigitation accounts for effective NP diameters smaller than the hydrodynamic size. For the 520 nm film after 168 h, the areal density is slightly greater than the RCP prediction. This behavior can be attributed to a further reduction in the interparticle spacing or the formation of 2D hexagonal packing (**Figure 5**, inset) that allows for a higher packing fraction (ca. 0.90) than the 2D RCP model (ca. 0.84).⁴⁵ Surface roughness can also enable a higher density at the surface than predicted by the 2D RCP model which assumes a flat surface. In summary, the areal density of NPs in the PMMA-NP-rich domains is about 40% greater than in the entire image for films with thicknesses of 520 nm and 1400 nm, consistent with observations for the 240 nm films.

Figure 5. Surface areal density of PMMA-NPs in 520 nm and 1400 nm films determined by AFM. The solid symbols represent the average density across an area of 2 μm 2 μm whereas the open symbols represent the density within the PMMA-NP-rich domains. The dotted and dashed lines represent theoretical limits from a 2D hard-sphere RCP model, assuming hydrodynamic and effective sphere diameters of 38 nm and 32 nm, respectively. The inset presents a cartoon for 2D hexagonal close packing, which has a higher volume fraction (ca. 0.90) than the random close packing (ca. 0.84).⁴⁵ Annealing times are included at the top within the figure for easy cross-reference with the text.

To capture lateral domain growth on the surface, correlation lengths, $\zeta(t)$, are determined using the radial autocorrelation function extracted from AFM images. $\zeta(t)$ represents the inter-domain distance. In **Figure 6**, $\zeta(t)$ is plotted as a function of the cube root of annealing time, $t^{1/3}$, for 520 nm and 1400 nm films. Phase separation begins within 1 h for 1400 nm films and 3 h for 520 nm, and continues for up to 10 h. During the initial period (t < 10 h), the correlation length scales linearly with $t^{1/3}$. For t > 10 h, the correlation length stabilizes at ca. 650 nm. This behavior aligns with prior theoretical and experimental investigations, which have shown that $\zeta(t)$ is proportional to $\left(\frac{t}{\eta}\right)^{1/3}$ during mid-stage phase separation driven by diffusive

droplet coalescence, where η is fluid viscosity.^{47,48,49} In the context of surface-directed spinodal decomposition (SDSD), domain growth asymptotically follows a $t^{1/3}$ scaling pattern in both perpendicular and parallel directions to the surface.⁵⁰ During late-stage phase separation, $\zeta(t)$ scales linearly with t, because domain coarsening accelerates due to hydrodynamic interactions.^{51,52} The observed $t^{1/3}$ scaling within the first 10 h is commensurate with the literature. For 520 nm and 1400 nm films, the linear slopes are similar, implying that film viscosity does not vary significantly when the film thicknesses are greater than 520 nm. Beyond 10 h, the constant correlation length indicates that the morphology is kinetically trapped and no longer undergoing significant evolution.

Figure 6. Correlation length measured from AFM images of 520 nm (blue pentagons) and 1400 nm (red diamonds) films annealed at 190 °C as a function of the cube root of annealing time. Dotted linear lines are fits to the correlation lengths for early times. For cross-reference with the text, annealing times are included across the top of the figure.

For the two thinnest films, the correlation lengths exhibit distinct trends. For 120 nm films after 1 h, the correlation length corresponds to a center-to-center interparticle distance of 43 nm

(half-filled square in **Figure 7**). Subsequently, $\zeta(t)$ maintains a nearly constant value of ca. 141 nm as the local height fluctuations (open squares in **Figure 7**) stop evolving with time. For 240 nm films annealed for 1 h and 3 h (open orange circles), the evolution of the $\zeta(t)$ is also attributed to height fluctuations. However, a transition occurs after 10 h, represented by the onset of phase separation into distinct PMMA-NP-rich and SAN-rich domains, denoted by the solid orange circles in **Figure 7**. During this stage, $\zeta(t)$ scales as $t^{1/2}$. Despite the bicontinuous structure at 10 h providing pathways for hydrodynamic flow, this $t^{1/2}$ scaling suggests that the underlying mechanism is neither diffusion-driven ($t^{1/3}$) nor hydrodynamic pumping (t^{1}).

Figure 7. Correlation length measured from AFM images of 120 nm (blue squares) and 240 nm (orange circles) films at 190 °C as a function of the square root of annealing time. For the 240 nm film, the correlation length increases linearly after 10 h. Open symbols represent correlation length between height fluctuations, whereas filled symbols correspond to lateral phase separation between PMMA-NP-rich and SAN-rich domains. The half-filled square represents the center-to-center interparticle distance of PMMA-NPs. Annealing times are included at the top for cross-reference with the text.

For 120 nm and 240 nm films, the distinct domain growth patterns arise from confinement due to film thickness. Krausch et al. studied surface-directed spinodal decomposition (SDSD) in films of a binary polymer mixture and found a characteristic thickness below which SDSD does not occur. This characteristic thickness was 1.5 times the spinodal wavelength.⁵³ Films constrained to this thickness range suppress SDSD and thus allow for a crossover from 3-dimensional (3D) to 2-dimensional (2D) behavior. Theoretical and numerical studies have shown that the late-stage coarsening exponent crosses over from 1 to a value near 0.46 when an off-critical fluid mixture with strong hydrodynamic interactions changes from 3D to 2D behavior. 47,54 Sung et al. experimentally confirmed this dimensional crossover by measuring the coarsening exponent ($n = 0.44 \pm 0.02$) for phase separation in polymer blend films below the characteristic thickness. 55 The observed domain growth scaling of $t^{1/2}$ for the 240 nm films in the present study agrees well with the literature, suggesting that the PMMA-NP/SAN film at this thickness is sufficiently thin to suppress SDSD. Additionally, for the 240 nm films, the correlation length at the onset of lateral phase separation, ca. 260 nm, serves as a useful estimate for the characteristic thickness separating 3D and 2D behavior. As film thickness further decreases to 120 nm, approximately 3-4 layers of PMMA-NPs in thickness, lateral phase separation ceases. This may be attributed to confinement effects previously observed in polymer blend films, where a miscibility window opens up due to a shift in the critical temperature for phase separation.⁵⁶

Surface Hydrophilicity. Water contact angle measurements are consistent with the surface morphology evolution observed using AFM. For thicknesses from 120 nm to 1400 nm, Figure 8 shows contact angle values (θ_m) plotted against the square root of annealing time to enhance visual representation. Additionally, average contact angles for a pure SAN film (ca. 78°) and

pure PMMA-NP film (ca. 66°) are plotted as dashed and dotted lines, respectively. Initially, the contact angles for the PNC films closely match the value for pure SAN films. Within experimental uncertainty, the trends for all thickness values are similar. After annealing, the contact angle gradually decreases until it approaches the value for pure PMMA-NP films after 168 h. This decrease in contact angle is commensurate with the increase in PMMA-NP areal density shown in **Figures 4** and **5**. Namely PMMA-NP areal density increases, the surface becomes more hydrophilic because the lower surface energy PMMA brush wets the surface.

Figure 8. Water contact angle values as a function of square root of annealing time for the 25/75 wt.% PMMA-NP/SAN films from 120 nm to 1400 nm annealed at 190 °C. For the 120 nm films, only contact angles for the stable films (t 24 h) are presented (c.f. **Figure 2d**). Dashed and dotted lines represent water contact angle values for pure SAN and pure PMMA-NP films, respectively.

The contact angle values are also quantitatively consistent with those predicted from AFM.

The areal percentage of PMMA-NP-rich domains is quantified using AFM height images and plotted against the square root of annealing time, as shown in the Supporting Information

(**Figure S4**). A rule of mixing relationship is used to predict contact angle values (θ_p) for the annealed PNC films that exhibit 2D phase separation,

$$\theta_p = A_{PMMA_NP} \theta_{PMMA_NP} + A_{SAN} \theta_{SAN}. \tag{2}$$

Here, A_{PMMA_NP} (or A_{SAN}) represent the areal ratio of PMMA-NP-rich (or SAN-rich) domains and θ_{PMMA_NP} (or θ_{SAN}) the contact angles for pure PMMA-NP (or SAN) films. The comparisons between the measured (θ_m) and predicted (θ_p) contact angles are plotted in **Figure 9** for thickness values of 240 nm (orange circles), 520 nm (green pentagons), and 1400 nm (red diamonds). The θ_p values (open symbols and dashed line) align well with θ_m (solid symbols and solid lines) for films annealed for up to 72 h. The observed discrepancy between θ_m and θ_p for films annealed for 168 h (highlighted in **Figure 9**) may be due to increased surface roughness at longer annealing times, a phenomenon also captured in the AFM images.

Figure 9. Comparison of experimentally measured water contact angles (, solid symbols) and predicted values (, open symbols). The predicted values are calculated using a rule of mixing (**Equation 2**). This comparison is applicable to annealed PNC films that undergo lateral phase separation. and are in good agreement except after 168 h samples (highlighted).

Surface Excess of PMMA-NPs. Concentration profiles of PMMA-NPs in the PNC films were established using ToF-SIMS. **Figure 10** displays Si⁺ concentration profiles as a function of depth for film thicknesses of 120 nm, 240 nm, 520 nm, and 1400 nm for selective annealing durations. Si⁺ was selected as the characteristic species to represent PMMA-NPs, as it is exclusively present in the silica core. To ensure an equilibrated sputtering rate at the PNC surface, a PS sacrificial layer (ca. 100 nm) was stacked on the PNC films post-annealing.³⁶ Si⁺ counts were normalized by the average counts in the bulk region, far away from the surface. To compensate for the

differential sputtering of the NPs and SAN, each depth profile was collected across a relatively large field of view (100 μ m × 100 μ m), which is more than two orders of magnitude larger than the domain sizes.³⁶ In the as-cast films (purple), Si⁺ profiles display a gradual, stepwise increase at the PNC surface and remain constant below the surface, consistent with a homogeneous distribution of PMMA-NPs within the bulk of the as-cast films. Upon annealing, a Si⁺ peak appears at the free surface, indicative of a PMMA-NP-rich layer at the surface and consistent with AFM height images in Figures 2 and 3. As time increases, the Si⁺ peaks grow in height (counts) and width (depth), due to the growth of the wetting layer in PNC films. For 520 nm and 1400 nm films, a depletion zone below the surface peak is observed after 1 h, as shown in Figure 10c and 10d, respectively. The depletion zone becomes less discernible due to phase separation in the near-surface region. For 520 nm and 1400 nm films, the depth of the wetting layer extends about 100 nm below the surface before reaching a plateau representative of the bulk concentration. For 120 nm and 240 nm films, the Si⁺ profiles from the surface and substrate wetting layers overlap in the middle of the film, obscuring the depletion zone. For the same film thicknesses (Figure 10a-b), the Si⁺ counts increase near the PNC/substrate interface. In as-cast films, this upturn is attributed solely to the native oxide layer on the substrate. For annealed films, this upturn is attributed to both the PMMA-NP wetting layer and the native silicon oxide laver.44

Figure 10. ToF-SIMS spectra of Si⁺ concentration profiles for 25/75 wt.% PMMA-NP/SAN films with thicknesses of 120 nm (a), 240 nm (b), 520 nm (c), and 1400 nm (d), annealed for various durations. Si⁺ is the characteristic species of the silica core in the PMMA-NPs. Counts are shifted vertically for clarity. The air/PNC surface is located near 0 nm.

The surface excess, Z^* , of the PMMA-NPs was extracted from the depth profiles to quantify the wetting behavior at the surface (**Figure 11**). Additional details regarding the determination of Z^* are found in Supporting Information (**Figure S5**). In the highly confined 120 nm films, Z^* stabilizes around 2.6 \pm 0.2 nm (dashed line) for annealing durations ranging from 1 h to 24 h. This observation indicates surface saturation of PMMA-NPs after 1 h, which is consistent with the areal density results shown in **Figure 4a**. For 520 nm and 1400 nm films, Z^* increases within the initial 10 h and then levels off, eventually converging towards a Z^* value of 2.6 nm, which is similar to the 120 nm case. The leveling off of Z^* after 10 h is consistent with the areal density

results in Figure 5. Note that the 120 nm film (Figure 4) has a slightly lower NP density at the surface than the 520 nm and 1400 nm films (Figure 5). Because ToF-SIMS integrates counts throughout the near-surface region, this discrepancy potentially arises from enhanced ordering below the top layer of NPs for the highly confined 120 nm films, which can increase the total NP surface excess. Because they probe different depths into the surface, further studies are needed to compare the areal density from AFM height images with the surface excess from ToF-SIMs. Interestingly, for the 240 nm films, Z^* increases with time and surpasses the values for other films. As noted previously, SDSD is suppressed when the film thickness is below the characteristic thickness, which is on the scale of the spinodal wavelength. In such thin films, spinodal waves originating from the surface and the substrate constructively interfere, leading to an enhanced surface excess. It is worth mentioning that this constructive interference in polymer blends implies a layered structure.⁵³ Thus for the 240 nm case, the PNC films are expected to exhibit a trilayer structure, with a middle SAN-rich domain sandwiched between PMMA-NP wetting layers – one at the surface and the other at the PNC/substrate interface. Furthermore, the overlap of the tail of the substrate wetting layer can enhance the Z^* measured at the surface. Further depth profiling is needed to investigate the enhanced surface wettings for the 240 nm films.

Figure 11. Surface excesses of PMMA-NPs for PNC films as a function of square root of annealing time. Film thicknesses are 240 nm (orange circle), 520 nm (green pentagon), and 1400 nm (red diamond). The blue dashed line (2.6 nm) represents the average surface excess value for annealed 120 nm films. Least-squares linear fittings were applied to the linear growth regime for the 520 nm (green solid line) and 1400 nm (red solid line) films. Annealing times are included at the top of the figure to simplify cross-referencing with the text.

The NP diffusion coefficient, D, can be extracted from the diffusion-limited linear growth regime ($t \le 10 h$) observed in the 520 nm and 1400 nm films. In this regime, Z^* is approximately proportional to $(Dt)^{1/2}$, in accordance with the law of mass conservation.⁴⁴ By applying least-squares linear regression (solid lines in **Figure 11**) to the corresponding Z^* values, the diffusion coefficients were determined to be 2.6×10^{-14} cm²/s for the 520 nm films and 2.7×10^{-14} cm²/s for 1400 nm films. These values are in good agreement with the previous result of 2.5×10^{-14} cm²/s obtained for 450 nm films of the same composition using ToF-SIMS.³⁶ These values, alongside the AFM results, confirm that the thickness dependence of the wetting characterized by NP areal density and NP surface excess becomes less significant for films thicker than 520 nm.

Bulk Structure. Film thickness plays an important role in determining the bulk structure of the 25/75 wt.% PMMA-NP/SAN films. Maguire et al. reported that PNC films with a thickness of approximately 450 nm exhibit vertical PMMA-NP pillars that span the film's thickness and connect the PMMA-NP wetting layers on the surface and the PNC/substrate interface. 44 In this section, we expand these studies to show how varying film thickness greater than 450 nm impacts the bulk structure of PNC films. Figure 12 presents cross-sectional TEM images for films of three different thicknesses, each subjected to four different annealing durations. Distinct morphologies are identified by different boundary outlines in these images. Prior to microtoming, the PNC films were sputter-coated with a gold/palladium layer, which is visible in some images (e.g., Figure 12e, i, j, l). For samples annealed for 1 h (black boxes), PMMA-NPs begin to form randomly oriented, elongated aggregates dispersed in the SAN phase, driven by bulk phase separation. After 24 h (orange boxes), these aggregates evolve into elongated pillars, oriented perpendicular to the film surface. Because the lateral dimension of the sample (ca. 10 mm × 10 mm) is much larger than the dimension perpendicular to the film surface (i.e., film thickness), PMMA-NP pillars and SAN phases tend to form vertical features to minimize interfacial contact between NP and SAN phases. Such phase separation patterns with vertical interfaces have also been observed in PMMA/SAN polymer blend films.³⁴ Analysis of the orientation angles of these PMMA-NP domains can be found in the Supporting Information (Figure S6). For 1400 nm films at 24 h, PMMA-NP pillars percolate the SAN phase and connect the wetting layers at the surface and interface. For thicker films (2400 nm and 4000 nm) at 24 h, the pillars become fragmented, possibly due to the limited diffusion distance that prevents NPs from forming larger domains required for the thicker films. After prolonged annealing (72 h and 168 h), the PMMA-NP domains coarsen into large, aggregated domains that are either

continuous networks (blue dashed boxes) or isolated clusters (blue solid boxes) for thicker and thinner films, respectively.

Figure 12. Cross-sectional TEM images of the 25/75 wt.% PMMA-NP/SAN films with various thicknesses and annealing times. For 24 h, orange arrows indicate the orientation of the PMMA-NP pillars, which are perpendicular to the film surface. Boxes around images represent distinct morphologies. Black-boxes denote discrete PMMA-NP aggregates. The orange dashed box denotes PMMA-NP pillars that span the entire thickness, while those in orange solid boxes show discontinuous PMMA-NP pillars. Images with solid blue boundaries show discrete, coarsened PMMA-NP domains. Dashed blue boxes represent continuous PMMA-NP networks. The darker lines on some images are gold/palladium layers for easier location under TEM.

Based on comprehensive cross-sectional TEM analysis, a morphology map as a function of film thickness and annealing time is constructed as shown in **Figure 13a**. This map identifies six distinct morphological regimes, labeled A-F, for thickness values from 450 nm³³ (horizontal dotted line) to 4000 nm. Initially, all as-cast films exhibit a uniform distribution of PMMA-NPs

across the film (regime A, c.f. Figure 1c). After 1 h, PMMA-NPs form disordered aggregates as well as wetting layers at the surface and substrate, represented as regime B. After 24 h, 1400 nm films display continuous PMMA-NP pillars, categorized as regime D and represented by solid upward triangles in Figure 13a. In contrast, 2400 nm and 4000 nm films show disconnected pillars, or regime C, marked by open triangles. In both regimes, the PMMA-NP pillars generally align perpendicular to the film surface as shown in **Figure 12b**, **f**, and **j**. With longer annealing, the pillars transition to an isotropic arrangement without a preferred orientation as shown in Figure S6 in the Supporting Information, giving rise to morphologies E and F as represented by open and solid squares in Figure 13a, respectively. A proposed transition mechanism from regime D to F is illustrated in Figure 13c. Similar to what is observed in polymer blend films, this transition can be attributed to the backflow of PMMA-NPs from the wetting layer into the bulk material. In regime D, capillary pressure forces PMMA-NPs to backflow from the wetting layers and the thin interconnecting channels between adjacent pillars, which leads to "necking" in the PMMA-NP domains and eventually the breakage of the pillars and the channels. As a result, SAN domains coalesce to form larger domains. Correspondingly, the PMMA-NP domains appear isolated within SAN phases or connected with the wetting layer, as seen in regime F. In thicker films (i.e., 2400 nm and 4000 nm), the isolated PMMA-NP pillars lose their directional orientation and coalesce with adjacent pillars, evolving into a network-like structure (regime E).

Figure 13. Cross-sectional morphology map of 25/75 wt.% PMMA-NP/SAN films as a function of annealing time and film thickness (a), featuring six distinct morphologies (denoted by different symbols and labeled A-F) that correspond to the cartoon schematics in (b). In these schematics, the orange circles represent PMMA-NPs, and the blue background represents the SAN phase. (c) provides a proposed mechanism elucidating the flow of PMMA-NPs as the morphology transitions from regime D to F with extended annealing. Here, the blue area represents the SAN phase, and the orange-dotted area represents the PMMA-NP domains.

CONCLUSIONS

In summary, we systematically investigated the film thickness dependence of the surface and bulk structures of PNC films consisting of PMMA-grafted silica nanoparticles in a SAN matrix. We show that the greatest confinement (120 nm) prevents lateral phase separation with NPs dispersed at a lower areal density than thicker films because of free energy minimization and matrix chain orientation propensity. Films thicker than 240 nm exhibit lateral phase separation and increased NP density at the surface with annealing time, approaching maxima calculated using a 2D random close-packing model for hard spheres. With increasing thickness, a

dimensional crossover of the correlation length behavior from 3D to 2D occurs for film thicknesses near 240 nm, suggesting a threshold thickness required to support surface-directed spinodal decomposition. For 520 nm and 1400 nm films, the correlation length scales as $t^{1/3}$ within the first 10 h, consistent with a diffusive droplet coalescence mechanism. Upon annealing, surface hydrophilicity steadily increases for all thicknesses, consistent with surface morphologies captured using AFM. Surface excesses measured from ToF-SIMS depth profiles (100 μ m × 100 μ m) are congruent with areal densities measured from AFM height images (2 μ m × 2 μ m).

A comprehensive morphology map for the PNC bulk structure as a function of film thickness and annealing time is constructed, identifying six unique morphology regimes. Within these regimes, PMMA-NPs transition from uniform dispersion in as-cast films to various aggregate forms, including pillars, networks, and NP domains encapsulated in SAN upon annealing. One goal of these studies was to identify conditions where long-lived vertical pillars observed in prior studies⁴⁴ become unstable such as regime C in Figure 13. Our results provide insights into a versatile strategy to control the spatial arrangement of NPs in PNCs by varying film thickness and annealing time. Future studies can focus on the structure-mechanical property relationship across the various morphologies unveiled in this study. Simulations and experiments can be conducted to examine the matrix chain orientation near the surface in the most confined 120 nm films, aiming to elucidate the origins of the confinement effect. Although the 120 nm films exhibit a lower NP surface density, their surface excess values are comparable to those of the 520 nm and 1400 nm films as determined from ToF-SIMS, which warrants further investigation. Additionally, the effects of particle size and brush height on the effect of confinement in composite films are of interest for future studies. Our study contributes to the understanding of materials design aimed at achieving desirable functional properties such as enhanced electric

conductivity and resistance to environmental degradation. Such advancements could enhance the performance of applications ranging from advanced barrier coatings to electronic and storage technologies.

MATERIALS AND METHODS

Materials

Our PNC system is poly(methyl methacrylate) – grafted silica nanoparticles (PMMA-NP) in a poly(styrene-ran-acrylonitrile) (SAN) matrix. The PMMA-NP has a brush molecular weight (Mw) of 19 kg/mol, a grafting density of 0.7 chains/nm², and a core silica diameter of 15 nm. SAN has a molecular weight (Mw) of 118 kg/mol and a polydispersity (M_w/M_n) of 2.24, with 33 wt.% acrylonitrile. The glass transition temperatures of the PMMA-NPs and SAN are determined to be 124 °C and 114 °C, respectively, using the differential scanning calorimeter (DSC) Q2000 from TA Instruments. Both PMMA-NPs and SAN were heated from 25 °C to 150 °C at a heating rate of 5 °C/min and cooled to 25 °C at the same rate. The measurement was repeated twice, and only the second cycle was used. SAN was provided by Monsanto and used after purification. To purify SAN, a solution of SAN and chloroform (≥ 99.9%, for HPLC) was added dropwise into methanol (≥ 99.9%, for HPLC) at a 1:10 volume ratio. SAN was allowed to precipitate for 1 h before the supernatant was removed using a pipette. The polymer was dried for 48 h in the air and purified once more using the same purification process. PMMA-NPs were prepared using surface-initiated atom transfer radical polymerization (ATRP).⁵⁷ To ensure all residual catalyst from the ATRP synthesis was removed, PMMA-NPs were dissolved in chloroform and washed using a solution of deionized water (100 mL) and Ethylenediaminetetraacetic acid disodium salt dihydrate (EDTA 2Na, 2 g) in a separatory funnel. The catalysis was extracted to the aqueous phase, and the organic phase was collected for the next round of washing. Washing was repeated

until the aqueous phase remained colorless after washing. The organic phase was then precipitated in n-Hexane (\geq 95 %, for HPLC), and PMMA-NPs were collected using a centrifuge. The PMMA-NPs collected were dried under vacuum for 24 h before storage. PS (Mn = 200 kg/mol, PDI = 1.07) was purchased from Polymer Source and used as received. Single-side-polished, P-type oriented silicon wafers (doped with boron, 0.001 – 0.005 Ω -cm resistivity, 500 μ m thickness) with a 300 nm wet thermal oxide layer were purchased from University Wafer. EpoxiCure 2 epoxy resin and hardener were purchased from Buehler.

Sample Preparation

A mixture of PMMA-NPs and SAN in a weight ratio of 25/75 was dissolved in methyl isobutyl ketone (MIBK) and stirred for 24 h. The PNC solutions, containing 4 wt.%, 10 wt.%, and 17 wt.% solids in MIBK, were spin-coated on silicon substrates, which were cleaned with methanol and toluene followed by 10 min of exposure to UV ozone before use. Spin-coating speed was varied to produce films with thicknesses ranging from 120 nm to 4000 nm. The films were then dried at 105 °C for 1 h to remove residual solvent. Film thicknesses were measured using Bruker Icon AFM. Samples were annealed on a hot stage (Mettler FP-82, Mettler Toledo, INC.) at 190 °C under a continuous argon flow for periods of 1 h, 3h, 10 h, 24 h, 72 h, 168 h, and then immediately quenched to room temperature.

Water Contact Angle Measurement

Water contact angle values reflect the surface enrichment of PMMA-NPs and indicate the thermal stability of films. Measurements of the water contact angle, as a function of film thickness and annealing time, are obtained using a home-built water contact angle goniometer. Using a Gilmont Micrometer Dispenser, a drop of deionized water was applied to the sample surface, which was illuminated by a Stocker and Yale Imagelite Lite Mite-Model 20 light source.

The snapshots of the droplets were captured using a Sony CCD Video Module N50 coupled with a Navitar Zoom 7000 Macro video lens. The images were then analyzed using LB-ADSA, a plugin for the ImageJ software, to measure the water contact angle. For each sample, three water contact angle measurements were taken at three distinct locations of the film.

Optical Microscope (OM)

An initial examination of the thermal stability of PNC films was conducted using Olympus BH2 optical microscope with a Lumenera 2-2 2 Megapixel CCD digital camera. The images were captured using a $10 \times$ and $20 \times$ objective lens and $1.67 \times$ relay lens.

Atomic Force Microscopy (AFM)

To study the surface enrichment of the PMMA-NPs, tapping-mode atomic force microscopy was performed on a Bruker Icon AFM, using HQ: HSC15/Al BS standard tapping mode AFM probes from MikroMasch. The AFM tapping mode tip coated in aluminum has a radius of less than 8 nm, and the cantilever has a force constant of 40 N/m and a resonance frequency of 325 kHz. AFM images were processed using NanoScope Analysis 2.0 and saved for subsequent analysis. Radial autocorrelation function for each image was obtained using the Gwyddion software. PMMA-NP number density and inter-domain distances were quantified using ImageJ software.

Time-of-Flight Secondary Ion Mass Spectrometry (ToF-SIMS)

To prepare samples for ToF-SIMS, a sacrificial polystyrene (PS) film was prepared and stacked on the PNC sample to ensure a consistent etching rate at the PNC surface during depth profiling. A PS solution (2 wt.% solids in toluene) was spin-coated (3000 rpm, 60 seconds) onto a silicon wafer to obtain films with a thickness of approximately 100 nm measured with a reflectometer (Filmetrics F3-UV). The PS film was then floated in a mixture of deionized water and sodium hydroxide solution (50 wt.%) at a volume ratio of 4:1, rinsed with deionized water, and stacked

onto as-cast or annealed PNC films. The assembled film was then annealed at 65 °C for 1 h to remove any residual moisture and eliminate wrinkles on the PS film.

Depth profiles were obtained using a TESCAN S8000X FIB/SEM equipped with a time-of-flight secondary ion mass analyzer. A 30 keV Xe⁺ ion plasma primary beam was used for both sputtering and analysis. Beam currents and analyzing areas were adjusted depending on the sample film thickness. A 3 nA Xe⁺ beam was used to sputter and analyze an area of 100 μ m × 100 μ m for 120 nm films, and 50 μ m × 50 μ m for 250 nm films, with sputtering rates of 0.07 nm/s and 0.4 nm/s, respectively. A 5 nA Xe⁺ beam was used for an area of 50 μ m × 50 μ m for films with thicknesses of 500 nm and 1400 nm, with corresponding sputtering rates of 0.6 nm/s and 0.7 nm/s. All depth profiles were collected with a normal primary beam. The dwell time was 10 μ s, and the resolution was 512 px × 512 px with a binning of 2 px × 2px. Si⁺ and C⁺ signals were chosen as the characteristic species for PMMA-NPs and polymers, respectively. Data collection was performed under an ultra-high vacuum with a pressure below 8×10⁻⁴ Pa using TOF-SIMS Explorer, version 1.12.2.0 software from Tofwerk AG. Frames were converted to depth based on the assumption that the sputtering rates for PS and PNC remained constant throughout each experiment.

Transmission Electron Microscope (TEM)

TEM was performed on the cross-sectional PNC film to investigate its bulk structure. The PNC film was subjected to similar floating and rinsing procedures as the PS film before being deposited on a Teflon® sheet. For top-down TEM imaging, the PNC was directly deposited on a TEM grid and dried in air before imaging. For cross-sectional TEM, the film was sputter-coated with a layer of gold/palladium to make the cross-sections easier to locate under the TEM. The sputter-coated films were then lifted off the Teflon® before being embedded in a two-part epoxy.

After curing for 48 h, the epoxy was cut into slices with an approximate thickness of 100 nm at

room temperature, using Leica Ultracut S Ultramicrotome with a diamond knife. The section was

then imaged using JEOL F200 scanning/transmission electron microscope. TEM images were

analyzed using ImageJ software.

SUPPORTING INFORMATION

The following information is included in one single PDF file:

Figure S1. An example of steps to process the TEM image for particle analysis using ImageJ.

Figure S2. A histogram of particle diameter distribution measured from the top-down TEM

image of the as-cast 120 nm film, fitted to a Gaussian function (blue curve).

Equation S1. Equation to calculate the polydispersity of nanoparticles.

Figure S3. AFM height image of the residual film inside the dewetted holes in the 120 nm film

annealed after 72 h (see the OM image in Figure 2) and line scans for measuring interparticle

distance.

Figure S4. Example of surface areal ratio determination of PMMA-NPs using AFM images and

the PMMA-NP areal ratio plotted against the square root of annealing time.

Figure S5. Example of surface excess, Z*, extraction from Si⁺ depth profiles for the 25/75 wt.%

PMMA-NP/SAN films.

Figure S6. Orientation angle distribution of TEM images for films with thicknesses of 1400 nm,

2400 nm, and 4000 nm, with various annealing times (c.f. Figure 12).

AUTHOR INFORMATION

Corresponding author

*Russell J. Composto – email: composto@seas.upenn.edu

Author Contributions

37

The manuscript was written through contributions of all authors. All authors have given approval to the final version of the manuscript. Aria C. Zhang was responsible for preparing the film samples, conducting the characterization experiments, and drafting the manuscript. Dr. Kohji Ohno contributed by providing the grafted nanoparticles used in the study.

ACKNOWLEDGEMENTS

This work was mainly funded by the NSF/DMR Polymers Program, DMR1905912 (RJC, ACZ). Polymer dynamics research was supported by NSF-PIRE-OISE-1545884 (RJC, ACZ), NSF-CBET2034122 (RJC), and NSF-NRT2152205 (RJC, ACZ). ACZ acknowledges support from the NSF Graduate Research Fellowship program. This work utilized characterization tools from the University of Pennsylvania's Nanoscale Characterization Facility, an NNCI member supported by NSF ECCS-1542153 and by NSF MRSEC-DMR-1720530.

The authors thank Dr. Douglas Yates, Dr. Jamie Ford, and Dr. Matthew Brukman for their help with using the JEOL F200 TEM-STEM, TESAN S8000X FIB-SEM, and Bruker Icon AFM at the University of Pennsylvania's Nanoscale Characterization Facility. The authors gratefully acknowledge helpful discussions with Dr. Shawn Maguire, Dr. Eric Stach, Dr. Karen I. Winey, and Dr. Robert A. Riggleman.

REFERENCE

- (1) Tannenbaum, R. J.; Cislo, N.; Ruzicka, E.; Dean, P. A.; Smith, Z. P.; Benicewicz, B. C.; Kumar, S. K. Activated Gas Transport in Polymer-Grafted Nanoparticle Membranes. *Macromolecules* **2023**, *56* (11), 3954–3961. https://doi.org/10.1021/acs.macromol.3c00215.
- (2) Bilchak, C. R.; Buenning, E.; Asai, M.; Zhang, K.; Durning, C. J.; Kumar, S. K.; Huang, Y.; Benicewicz, B. C.; Gidley, D. W.; Cheng, S.; Sokolov, A. P.; Minelli, M.; Doghieri, F. Polymer-Grafted Nanoparticle Membranes with Controllable Free Volume. *Macromolecules* 2017, 50 (18), 7111–7120. https://doi.org/10.1021/acs.macromol.7b01428.
- (3) Fang, Y.; Tong, J.; Qiu, S. Bioinspired Strong and Tough Poly(ε-Caprolactone)/Graphene Nanodot Composite Films via Weak Hydrogen Bonds: Implications for Thermal–Mechanical Properties. *ACS Appl. Nano Mater.* **2023**, *6* (20), 19088–19097. https://doi.org/10.1021/acsanm.3c03613.
- (4) Kumar, S. K.; Jouault, N.; Benicewicz, B.; Neely, T. Nanocomposites with Polymer Grafted Nanoparticles. *Macromolecules* 2013, 46 (9), 3199–3214. https://doi.org/10.1021/ma4001385.
- (5) Kumar, S. K.; Benicewicz, B. C.; Vaia, R. A.; Winey, K. I. 50th Anniversary Perspective: Are Polymer Nanocomposites Practical for Applications? *Macromolecules* 2017, 50 (3), 714–731. https://doi.org/10.1021/acs.macromol.6b02330.
- (6) Zhang, L.; Bei, H. P.; Piao, Y.; Wang, Y.; Yang, M.; Zhao, X. Polymer-Brush-Grafted Mesoporous Silica Nanoparticles for Triggered Drug Delivery. *ChemPhysChem* 2018, 19 (16), 1956–1964. https://doi.org/10.1002/cphc.201800018.

- (7) Chancellor, A. J.; Seymour, B. T.; Zhao, B. Characterizing Polymer-Grafted Nanoparticles: From Basic Defining Parameters to Behavior in Solvents and Self-Assembled Structures. *Anal. Chem.* **2019**, *91* (10), 6391–6402. https://doi.org/10.1021/acs.analchem.9b00707.
- (8) Tawade, B. V.; Singh, M.; Apata, I. E.; Veerasamy, J.; Pradhan, N.; Karim, A.; Douglas, J. F.; Raghavan, D. Polymer-Grafted Nanoparticles with Variable Grafting Densities for High Energy Density Polymeric Nanocomposite Dielectric Capacitors. *JACS Au* 2023, 3 (5), 1365–1375. https://doi.org/10.1021/jacsau.3c00022.
- (9) Winey, K. I.; Vaia, R. A. Polymer Nanocomposites. MRS Bull. 2007, 32 (4), 314–322. https://doi.org/10.1557/mrs2007.229.
- (10) Winey, K. I.; Kashiwagi, T.; Mu, M. Improving Electrical Conductivity and Thermal Properties of Polymers by the Addition of Carbon Nanotubes as Fillers. *MRS Bull.* 2007, 32
 (4), 348–353. https://doi.org/10.1557/mrs2007.234.
- (11) Kojima, Y.; Usuki, A.; Kawasumi, M.; Okada, A.; Fukushima, Y.; Kurauchi, T.; Kamigaito,
 O. Mechanical Properties of Nylon 6-Clay Hybrid. *J. Mater. Res.* 1993, 8 (5), 1185–1189.
 https://doi.org/10.1557/JMR.1993.1185.
- (12) Akcora, P.; Liu, H.; Kumar, S. K.; Moll, J.; Li, Y.; Benicewicz, B. C.; Schadler, L. S.; Acehan, D.; Panagiotopoulos, A. Z.; Pryamitsyn, V.; Ganesan, V.; Ilavsky, J.; Thiyagarajan, P.; Colby, R. H.; Douglas, J. F. Anisotropic Self-Assembly of Spherical Polymer-Grafted Nanoparticles. *Nat. Mater.* 2009, 8 (4), 354–359. https://doi.org/10.1038/nmat2404.
- (13) Hore, M. J. A.; Composto, R. J. Functional Polymer Nanocomposites Enhanced by Nanorods. *Macromolecules* **2014**, *47* (3), 875–887. https://doi.org/10.1021/ma402179w.
- (14) Hore, M. J. A. Polymers on Nanoparticles: Structure & Dynamics. *Soft Matter* **2019**, *15* (6), 1120–1134. https://doi.org/10.1039/C8SM02110D.

- (15) Meli, L.; Arceo, A.; Green, P. F. Control of the Entropic Interactions and Phase Behavior of Athermal Nanoparticle/Homopolymer Thin Film Mixtures. *Soft Matter* **2009**, *5* (3), 533–537. https://doi.org/10.1039/B814714K.
- (16) Arceo, A.; Meli, L.; Green, P. F. Glass Transition of Polymer–Nanocrystal Thin Film Mixtures: Role of Entropically Directed Forces on Nanocrystal Distribution. *Nano Lett.* 2008, 8 (8), 2271–2276. https://doi.org/10.1021/nl800932u.
- (17) Green, P. F. The Structure of Chain End-Grafted Nanoparticle/Homopolymer Nanocomposites. *Soft Matter* **2011**, *7* (18), 7914. https://doi.org/10.1039/c1sm05076a.
- (18) Chevigny, C.; Dalmas, F.; Di Cola, E.; Gigmes, D.; Bertin, D.; Boué, F.; Jestin, J. Polymer-Grafted-Nanoparticles Nanocomposites: Dispersion, Grafted Chain Conformation, and Rheological Behavior. *Macromolecules* 2011, 44 (1), 122–133. https://doi.org/10.1021/ma101332s.
- (19) Srivastava, S.; Agarwal, P.; Archer, L. A. Tethered Nanoparticle–Polymer Composites:

 Phase Stability and Curvature. *Langmuir* **2012**, *28* (15), 6276–6281.

 https://doi.org/10.1021/la2049234.
- (20) Xu, C.; Ohno, K.; Ladmiral, V.; Composto, R. J. Dispersion of Polymer-Grafted Magnetic Nanoparticles in Homopolymers and Block Copolymers. *Polymer* **2008**, *49* (16), 3568–3577. https://doi.org/10.1016/j.polymer.2008.05.040.
- (21) Zhang, R.; Lee, B.; Bockstaller, M. R.; Kumar, S. K.; Stafford, C. M.; Douglas, J. F.; Raghavan, D.; Karim, A. Pattern-Directed Phase Separation of Polymer-Grafted Nanoparticles in a Homopolymer Matrix. *Macromolecules* 2016, 49 (10), 3965–3974. https://doi.org/10.1021/acs.macromol.6b00228.

- (22) Martin, T. B.; Mongcopa, K. I. S.; Ashkar, R.; Butler, P.; Krishnamoorti, R.; Jayaraman, A. Wetting–Dewetting and Dispersion–Aggregation Transitions Are Distinct for Polymer Grafted Nanoparticles in Chemically Dissimilar Polymer Matrix. *J. Am. Chem. Soc.* 2015, 137 (33), 10624–10631. https://doi.org/10.1021/jacs.5b05291.
- (23) Koski, J. P.; Krook, N. M.; Ford, J.; Yahata, Y.; Ohno, K.; Murray, C. B.; Frischknecht, A. L.; Composto, R. J.; Riggleman, R. A. Phase Behavior of Grafted Polymer Nanocomposites from Field-Based Simulations. *Macromolecules* 2019, 52 (14), 5110–5121. https://doi.org/10.1021/acs.macromol.9b00720.
- (24) Santos, A. P.; Frischknecht, A. L. Phase Behavior of Polymer-Grafted Nanoparticles in Homopolymer Blends from Simulations. *Macromolecules* **2022**, *55* (23), 10245–10254. https://doi.org/10.1021/acs.macromol.2c01684.
- (25) Jandt, K. D.; Heier, J.; Bates, F. S.; Kramer, E. J. Transient Surface Roughening of Thin Films of Phase Separating Polymer Mixtures. *Langmuir* **1996**, *12* (15), 3716–3720. https://doi.org/10.1021/la950753c.
- (26) Jones, R. A. L.; Norton, L. J.; Kramer, E. J.; Bates, F. S.; Wiltzius, P. Surface-Directed Spinodal Decomposition. *Phys. Rev. Lett.* **1991**, *66* (10), 1326–1329. https://doi.org/10.1103/PhysRevLett.66.1326.
- (27) Newby, B. Z.; Composto, R. J. Influence of Lateral Confinement on Phase Separation in Thin Film Polymer Blends. *Macromolecules* **2000**, *33* (9), 3274–3282. https://doi.org/10.1021/ma992092m.
- (28) Krausch, G. Surface Induced Self Assembly in Thin Polymer Films. *Mater. Sci. Eng. R Rep.* **1995**, *14* (1), v–94. https://doi.org/10.1016/0927-796X(94)00173-1.

- (29) Gam, S.; Corlu, A.; Chung, H.-J.; Ohno, K.; Hore, M. J. A.; Composto, R. J. A Jamming Morphology Map of Polymer Blend Nanocomposite Films. *Soft Matter* **2011**, 7 (16), 7262–7268. https://doi.org/10.1039/C1SM05619K.
- (30) Chung, H.; Ohno, K.; Fukuda, T.; Composto, R. J. Internal Phase Separation Drives Dewetting in Polymer Blend and Nanocomposite Films. *Macromolecules* **2007**, *40* (2), 384–388. https://doi.org/10.1021/ma062024h.
- (31) Binder, K. Phase Transitions of Polymer Blends and Block Copolymer Melts in Thin Films.
 In *Polymers in Confined Environments*; Granick, S., Binder, K., de Gennes, P.-G.,
 Giannelis, E. P., Grest, G. S., Hervet, H., Krishnamoorti, R., Léger, L., Manias, E., Raphaël,
 E., Wang, S.-Q., Eds.; Springer: Berlin, Heidelberg, 1999; pp 1–89.
 https://doi.org/10.1007/3-540-69711-X 1.
- (32) Chandran, S.; Begam, N.; Padmanabhan, V.; Basu, J. K. Confinement Enhances Dispersion in Nanoparticle–Polymer Blend Films. *Nat. Commun.* 2014, 5 (1), 3697. https://doi.org/10.1038/ncomms4697.
- (33) Maguire, S. M.; McClimon, J. B.; Zhang, A. C.; Keller, A. W.; Bilchak, C. R.; Ohno, K.; Carpick, R. W.; Composto, R. J. Nanoscale Structure–Property Relations in Self-Regulated Polymer-Grafted Nanoparticle Composite Structures. *ACS Appl. Mater. Interfaces* 2023, *15* (8), 10974–10985. https://doi.org/10.1021/acsami.2c15786.
- (34) Chung, H.; Wang, H.; Composto, R. J. A Morphology Map Based on Phase Evolution in Polymer Blend Films. *Macromolecules* **2006**, *39* (1), 153–161. https://doi.org/10.1021/ma051513z.
- (35) Hariharan, A.; Kumar, S. K.; Rafailovich, M. H.; Sokolov, J.; Zheng, X.; Duong, D.; Schwarz, S. A.; Russell, T. P. The Effect of Finite Film Thickness on the Surface

- Segregation in Symmetric Binary Polymer Mixtures. *J. Chem. Phys.* **1993**, *99* (1), 656–663. https://doi.org/10.1063/1.465738.
- (36) Zhang, A. C.; Maguire, S. M.; Ford, J. T.; Composto, R. J. Using Focused Ion Beam Time-of-Flight Secondary Ion Mass Spectrometry to Depth Profile Nanoparticles in Polymer Nanocomposites. *Microsc. Microanal.* 2023, 29 (5), 1557-1565. https://doi.org/10.1093/micmic/ozad085.
- (37) Wang, A.; De Silva, K.; Jones, M.; Robinson, P.; Larribe, G.; Gao, W. Anticorrosive Coating Systems for Marine Propellers. *Prog. Org. Coat.* **2023**, *183*, 107768. https://doi.org/10.1016/j.porgcoat.2023.107768.
- (38) Sahore, R.; Armstrong, B. L.; Tang, X.; Liu, C.; Owensby, K.; Kalnaus, S.; Chen, X. C. Role of Scaffold Architecture and Excess Surface Polymer Layers in a 3D-Interconnected Ceramic/Polymer Composite Electrolyte. *Adv. Energy Mater.* 2023, *13* (19), 2203663. https://doi.org/10.1002/aenm.202203663.
- (39) Maréchal, M.; Niepceron, F.; Gebel, G.; Mendil-Jakani, H.; Galiano, H. Inside the Structure of a Nanocomposite Electrolyte Membrane: How Hybrid Particles Get along with the Polymer Matrix. *Nanoscale* **2015**, *7* (7), 3077–3087. https://doi.org/10.1039/C4NR05330C.
- (40) Li, R.; Bulucu, D.; Chou, T.; Akcora, P. Enhanced Ion Conductivity in a Poly(Ionic Liquid)-Grafted Nanoparticle-Based Single-Ion Conductor. *Macromolecules* 2024, 57 (8), 3807–3815. https://doi.org/10.1021/acs.macromol.3c02623.
- (41) Irani, R. R. *Particle Size: Measurement, Interpretation and Application*; Wiley: New York, 1963.
- (42) Maguire, S. M.; Krook, N. M.; Kulshreshtha, A.; Bilchak, C. R.; Brosnan, R.; Pana, A.-M.; Rannou, P.; Maréchal, M.; Ohno, K.; Jayaraman, A.; Composto, R. J. Interfacial

- Compatibilization in Ternary Polymer Nanocomposites: Comparing Theory and Experiments. *Macromolecules* **2021**, *54* (2), 797–811. https://doi.org/10.1021/acs.macromol.0c02345.
- (43) Seemann, R.; Herminghaus, S.; Jacobs, K. Dewetting Patterns and Molecular Forces: A Reconciliation. *Phys. Rev. Lett.* **2001**, *86* (24), 5534–5537. https://doi.org/10.1103/PhysRevLett.86.5534.
- (44) Maguire, S. M.; Boyle, M. J.; Bilchak, C. R.; Demaree, J. D.; Keller, A. W.; Krook, N. M.; Ohno, K.; Kagan, C. R.; Murray, C. B.; Rannou, P.; Composto, R. J. Grafted Nanoparticle Surface Wetting during Phase Separation in Polymer Nanocomposite Films. *ACS Appl. Mater. Interfaces* 2021, *13* (31), 37628–37637. https://doi.org/10.1021/acsami.1c09233.
- (45) Meyer, S.; Song, C.; Jin, Y.; Wang, K.; Makse, H. A. Jamming in Two-Dimensional Packings. *Phys. Stat. Mech. Its Appl.* **2010**, *389* (22), 5137–5144. https://doi.org/10.1016/j.physa.2010.07.030.
- (46) Schmidt, I.; Binder, K. Model Calculations for Wetting Transitions in Polymer Mixtures. *J. Phys.* **1985**, *46* (10), 1631–1644. https://doi.org/10.1051/jphys:0198500460100163100.
- (47) San Miguel, M.; Grant, M.; Gunton, J. D. Phase Separation in Two-Dimensional Binary Fluids. *Phys. Rev. A* **1985**, *31* (2), 1001–1005. https://doi.org/10.1103/PhysRevA.31.1001.
- (48) Lifshitz, I. M.; Slyozov, V. V. The Kinetics of Precipitation from Supersaturated Solid Solutions. *J. Phys. Chem. Solids* **1961**, *19* (1), 35–50. https://doi.org/10.1016/0022-3697(61)90054-3.
- (49) Chung, H.-J.; Taubert, A.; Deshmukh, R. D.; Composto, R. J. Mobile Nanoparticles and Their Effect on Phase Separation Dynamics in Thin-Film Polymer Blends. *Europhys. Lett.* **2004**, *68* (2), 219. https://doi.org/10.1209/epl/i2004-10242-2.

- (50) Brown, G.; Chakrabarti, A. Surface-Directed Spinodal Decomposition in a Two-Dimensional Model. *Phys. Rev. A* **1992**, *46* (8), 4829–4835. https://doi.org/10.1103/PhysRevA.46.4829.
- (51) Wang, H.; Composto, R. J. Hydrodynamic-Flow-Driven Wetting in Thin Film Polymer Blends: Growth Kinetics and Morphology. *Phys. Rev. E* **2000**, *61* (2), 1659–1663. https://doi.org/10.1103/PhysRevE.61.1659.
- (52) Siggia, E. D. Late Stages of Spinodal Decomposition in Binary Mixtures. *Phys. Rev. A* **1979**, *20* (2), 595–605. https://doi.org/10.1103/PhysRevA.20.595.
- (53) Krausch, G.; Dai, C.-A.; Kramer, E. J.; Bates, F. S. Spinodal Decomposition in Thin Polymer Films. *Berichte Bunsenges. Für Phys. Chem.* **1994**, *98* (3), 446–448. https://doi.org/10.1002/bbpc.19940980338.
- (54) Wu, Y.; Alexander, F. J.; Lookman, T.; Chen, S. Effects of Hydrodynamics on Phase Transition Kinetics in Two-Dimensional Binary Fluids. *Phys. Rev. Lett.* **1995**, *74* (19), 3852–3855. https://doi.org/10.1103/PhysRevLett.74.3852.
- (55) Sung, L.; Karim, A.; Douglas, J. F.; Han, C. C. Dimensional Crossover in the Phase Separation Kinetics of Thin Polymer Blend Films. *Phys. Rev. Lett.* **1996**, *76* (23), 4368–4371. https://doi.org/10.1103/PhysRevLett.76.4368.
- (56) Reich, S.; Cohen, Y. Phase Separation of Polymer Blends in Thin Films. J. Polym. Sci. Polym. Phys. Ed. 1981, 19 (8), 1255–1267. https://doi.org/10.1002/pol.1981.180190809.
- (57) Ohno, K.; Morinaga, T.; Koh, K.; Tsujii, Y.; Fukuda, T. Synthesis of Monodisperse Silica Particles Coated with Well-Defined, High-Density Polymer Brushes by Surface-Initiated Atom Transfer Radical Polymerization. *Macromolecules* 2005, 38 (6), 2137–2142. https://doi.org/10.1021/ma048011q.